RSC Advances

PAPER

View Article Online
View Journal | View Issue

Cite this: *RSC Adv.*, 2020, **10**, 12423

A 3D nitrogen-doped graphene aerogel for enhanced visible-light photocatalytic pollutant degradation and hydrogen evolution

Chanez Maouche,[a] Yazhou Zhou,[a] Jinjun Peng,[a] Shuang Wang,[a] Xiujuan Sun,[a] Nasir Rahman,[a] Piyaphong Yongphet,[b] Qinqin Liu[a] and Juan Yang *[a]

Received 20th February 2020
Accepted 11th March 2020

DOI: 10.1039/d0ra01630f

rsc.li/rsc-advances

Three-dimensional (3D) graphene-based aerogels have attracted widespread interest as promising photocatalysts for dye degradation and hydrogen production. Herein, we have developed a 3D nitrogen-doped graphene aerogel (3DNG) from graphitic carbon nitride combined with graphene oxide (GO). The nitrogen dopant in the 3D aerogel was achieved *via* a thermal treatment at 1000 °C, and the 3D aerogel catalyst could retain its 3D porous structure after the thermal treatment. The 3DNG was characterized *via* FTIR, Raman, TEM, UV-vis, XPS spectroscopies and BET analysis, and the results indicated that this 3DNG with a large surface area of 536 m^2 g^{-1} and a band gap of 2.42 eV demonstrated a high adsorption capacity and enhanced methylene blue degradation and hydrogen production under visible light irradiation. Characterization also identified that the porous 3D structure with hydrogen bonding and $\pi-\pi$ interactions and better charge transfer resulting from the nitrogen doping are the major reasons for the enhanced photocatalytic performance over this 3DNG catalyst.

Introduction

The rapid population growth and development of industries have contributed to increase the energy demand and elevate the levels of dangerous pollutants in the environment. This further contribute to climate change and presents a serious threat to all life forms, thus necessitating reductions in the consumption of conventional energy sources.[1] As a consequence, numerous efforts have been dedicated to solve those problems, and photocatalysis technology driven by solar energy has attracted widespread attention from scientists for the removal of pollutants and the generation of clean energy, namely hydrogen (H_2).[2–5] Many photocatalyst materials have been developed such as zinc oxide (ZnO), cadmium sulfide (CdS), titanium oxide (TiO_2), *etc.*, and have been applied to mitigate the problem of dye pollutants in water[6,7] and to generate H_2 from water splitting. However, their low quantum efficiencies and insufficient exposure of actives sites hinder their photocatalytic applications.[2]

Recently, graphene, a typical two-dimensional (2D) carbon material, has been demonstrated to be an alternative and cost-effective photocatalyst for both dye degradation and H_2 evolution, since carbon is abundant and environmentally friendly.[8,9] Compared to other traditional photocatalysts, graphene is composed of sp^2-hybridized sheets linked by van der Waals bonds, which has special properties including high surface area, large π-conjugation system, high electron mobility, efficient light-harvesting, and many adjustable defect-density active sites.[10] Many studies have proved that photocatalytic systems with graphene tend to offer additional active sites and increase the active surface area so as to increase the charge transport and thus achieve high photocatalytic performance.[11,12] Compared with 2D graphene nanosheets, three-dimensional (3D) graphene aerogels with an interconnected nanosheet structure demonstrate a larger surface area and hierarchical porous structure, which is more conducive to expose more active sites and providing high structural stability for the photocatalytic reaction.[13] However, pristine 3D graphene aerogels usually demonstrate insufficient photocatalytic activity toward dye degradation and H_2 evolution. Heteroatom doping into the graphene lattice has been evidenced as an effective method for modifying the electronic structure, promoting charge transfer, extending light absorbers from UV to visible light and forming semiconductors. For example, Teng *et al.*[8] synthesized nitrogen-doped graphene quantum dots and proved that they can realize overall photocatalytic water-splitting. Despite the widespread interest in using graphene materials as photocatalysts for hydrogen production and the degradation of dye pollutants, there are still few reports of these materials for hydrogen production. Some reports have demonstrated that N-doped graphene can generate H_2 under UV light;[14] however, visible light represents 40% of the solar spectrum and thus the development of catalysts with high absorption in the visible light

[a]*School of Materials Science and Engineering, Jiangsu University, Zhenjiang, Jiangsu, 212013, P. R. China. E-mail: yangjuan6347@ujs.edu.cn*

[b]*School of Energy and Power Engineering, Jiangsu University, Zhenjiang, Jiangsu, 212013, P. R. China*

spectrum region and the ability to generate H_2 is highly desirable for the development of solar energy. Although there have been reports on 3D N-doped graphene,[15] the H_2 generation was not investigated. As such, exploration of 3D N-doped graphene for hydrogen production and as a photocatalyst for dye degradation under visible light is attractive.

To prepare nitrogen-doped graphene, the choice of an appropriate nitrogen source is very important. Graphitic carbon nitride (g-C_3N_4), is another typical 2D carbon material and is known to be a nitrogen-rich compound. Furthermore, g-C_3N_4 decomposes to NH_3, N_2 and N-group moieties at around 725 °C, indicating that it can be employed as a nitrogen source in order to achieve nitrogen doping in graphene.[16,17] In view of the discussion above, we aimed to synthesize a 3D-nitrogen doped graphene aerogel from graphene oxide and g-C_3N_4 as the nitrogen source. Taking advantage of nitrogen doping and the 3D aerogel structure, the 3D-nitrogen-doped graphene aerogel has demonstrated efficient photocatalytic performance in methylene blue (MB) degradation and H_2 evolution. The photocatalytic mechanism for MB degradation and H_2 evolution has been studied in this work.

Experimental and characterization

Materials

Urea and methylene blue trihydrate, both with purity of over 99% were obtained from Sinopharm Chemical Reagent Co. Ltd. Ascorbic acid with over 99% purity was obtained from Aladdin Industrial Corporation. All the chemicals were used as obtained and were not subjected to further purification.

Preparation of graphene oxide

A modified Hummers' method was used to synthesize graphene oxide.[18] To a solution containing 12.5 mL of H_2SO_4, 2.5 mg of $K_2S_2O_8$ and 2.5 mg of P_2O_5 at 80 °C, 3 g of graphite powder was added. After 6 hours, 500 mL of H_2O was added to dilute the mixture, which was then filtered with a 0.2 μm nylon millipore filter and washed before being dried overnight under an air atmosphere. Next, 115 mL of H_2SO_4 was placed in an ice bath at a temperature of 0 °C, to which the oxidized graphite was introduced with shaking. At a temperature of 10 °C, 15 g of $KMnO_4$ was added gradually and the mixture was reacted at 35 °C for 2 h. In order to maintain a temperature below 50 °C, 230 mL of distilled was added. After 2 h, 700 mL of H_2O and 12.5 mL of 30% H_2O_2 were introduced and the color of the mixture changed to yellow with the appearance of bubbles. The mixture remaining after decantation was centrifuged and washed again in 10% of HCl, then with 1.25 L of H_2O to eliminate the acid, followed by dialysis of the solid to remove any metallic and iron oxide particles to give graphene oxide.

Synthesis of 3D nitrogen-doped graphene aerogel

The g-C_3N_4 (62.1 mg, synthesized as reported[19]) was dispersed in 6.21 mL of distilled water by ultrasonication for 6 hours. The dispersed solution was added to 3.72 mL (2.5 mg L^{-1}) of GO before further ultrasonication for 2 h. Then, 37.2 mg of urea and 9.3 mg of ascorbic acid (as a reductant) were added and dispersed in the above solution for about 1 h. The solution was sealed and maintained at 180 °C for 6 h in a Teflon-lined autoclave and was allowed to cool naturally. During this process, the GO combined with g-C_3N_4 and formed 3D porous reduced GO (rGO), where the 3D graphene-based hydrogel was obtained as shown in Fig. 1(a). The 3D aerogel was established after freeze-drying the 3D hydrogel and then heated for 1 h under an Ar atmosphere at 1000 °C (2 °C min^{-1}). The thermally treated 3D nitrogen-doped graphene aerogel was obtained (3DNG) as shown in Fig. 1(b).

Characterization

Fourier transform infrared spectroscopy (FT-IR) was performed on a Nicolet Nexus 470 instrument. Raman spectroscopy was carried out on Laser Raman spectrometer DXR (Thermo Fisher). Powder X-ray diffraction (XRD, Rigaku Smartlab X-ray diffractometer, Cu Kα, $\lambda = 1.54$ Å) and X-ray photoelectron spectroscopy (XPS, Thermo ESCALAB 250Xi spectrometer, monochromatic X-ray source) were used to investigate the structure and the chemistry on the surface of the catalyst. The sample morphology was observed by a transmission electron microscope (TEM) equipped with a selected area diffraction (SAED) system, controlled at an accelerating voltage of 200 kV on a JEOL JSM-2100F.

The Brunauer–Emmett–Teller (BET) surface area and pore size distribution were defined on a Quantachrome Nova 3000e adsorption instrument. The UV-visible spectrophotometer (DRS, UV-2600) was used to measure the UV-vis diffuse reflectance spectra. A CHI-660E workstation (Shanghai, China) was used to carry out the photochemical measurements including transient photocurrent reponses, electrochemical impedance (EIS), and Mott–Schottky plots (M–S). These measurements were done using a standard three-electrode system, where the prepared catalysts, a platinum plate and Ag/AgCl were the working electrode, counter electrode and reference electrode, respectively, with 0.5 M Na_2SO_4 solution as the electrolyte (pH = 6.8). To activate the working electrode in order to proceed to the tests, 5 mg of catalyst was dispersed in 250 μL of ethylene blue and 40 μL of membrane dissolution D520 over ITO glass substrate, then were dried in the oven in 70 °C for 2 h using 365 nm UV LED spot curing lamp (Model UVEC-4 II).

Adsorption experiment

Adsorption experiments were performed using methylene blue aqueous solution. The experiments were performed in 250 mL beakers by adding 10 mg of samples to a series of dye solutions with different concentrations (100 mL, 5–25 mg L^{-1}). The suspension was stirred in the dark for 150 min using a magnetic stirrer. The solution was then centrifuged. After that, a UV-vis spectrophotometer (Shimadzu UV-2600 spectrophotometer, Japan) was used to measure the concentration of methylene blue. Eqn (1) was used to calculate the adsorption at time t, q_t (mg g^{-1}):

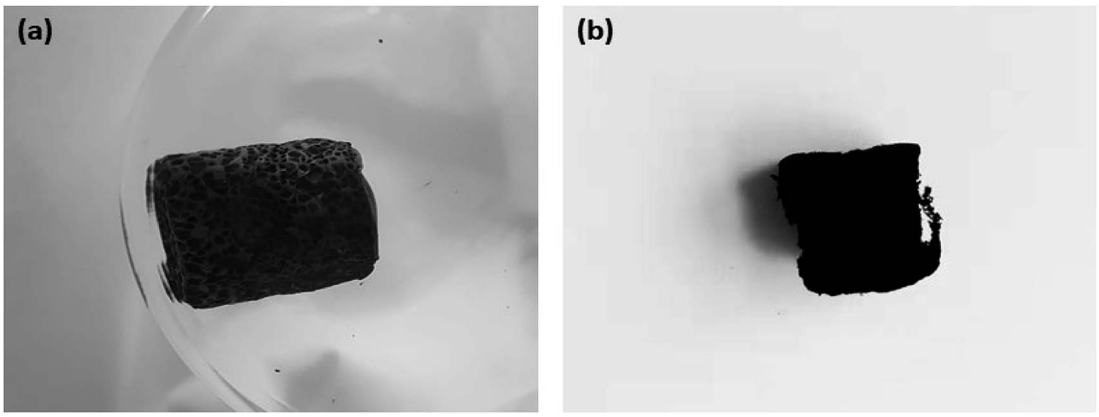

Fig. 1 Photographs of (a) the 3D aerogel, and (b) 3DNG.

$$q_t = \frac{(C_0 - C_t)\ V}{W} \quad (1)$$

C_0 (mg L^{-1}) represents the initial concentration of the dye, C_t is the concentration of the dye at a specific time t, V represents the volume of the dye solution (L) and W is the weight of the photocatalyst used (g).

Photocatalytic activity test

The photocatalytic degradation activities of GO and 3DNG were carried out using methylene blue (MB) as the target dye under UV-vis light and an air atmosphere. In 100 mL of aqueous solution of MB, 1 mg of the photocatalyst was suspended in the dark and agitated for 0.3 h to reach adsorption/desorption equilibrium. The solution was irradiated from 15 cm away by xenon lamps. The absorbance of the mixture was monitored at 663 nm for photodegradation.

The photocatalytic H_2 production was conducted under the irradiation of a 350 W xenon lamp in a triple necked round-bottom flask; 15 mg of each sample was dispersed in a mixture solution of 80 mL distilled water, 8 mL triethanolamine and 20 μL H_2PtCl_6. Before light irradiation, the solution was filled with N_2 to remove all the air. Gas evolution was measured by extracting 0.4 mL of gaseous products after 1 h over 3 h using a gas chromatograph (GC-2014, Shimadzu, Japan).

Results and discussion

Raman spectroscopy is an important tool for investigating the nitrogen doping and disorder in the graphene. As shown in Fig. 2(a), both GO and 3DGN samples displayed two distinctive peaks at approximately 1345 cm^{-1} and 1580 cm^{-1}, attributed to the D and G bands, respectively. The D band shows defects resulting from the vibration of the sp^3 carbon structure, and the G band can be associated with the E_{2g} mode of single graphitic sp^2 carbon atoms.[20] The intensity ratio of I_D/I_G gives information about the degree of disorder of graphene.[21] The increase in the I_D/I_G ratio from 0.96 to 1.04 indicated the structure disorder and defects in the 3DNG, which may be due to the nitrogen doping.[22] FT-IR spectroscopy was used to identify the functional groups of 3DNG and GO (Fig. 2(b)). GO exhibited a characteristic band at 3375 cm^{-1}, which corresponds to O–H groups. The bands at 1725 cm^{-1} and 1622 cm^{-1} were assigned to the

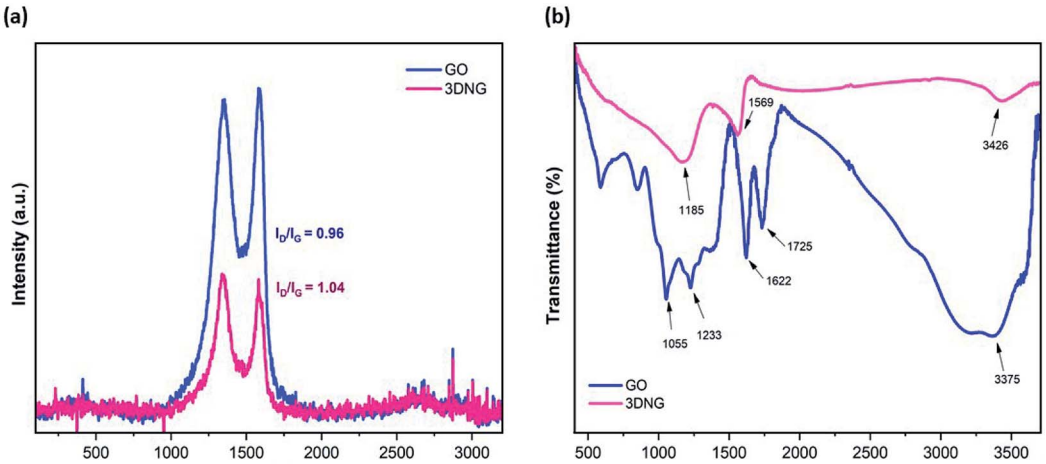

Fig. 2 (a) Raman and (b) FTIR spectra of GO and 3DNG.

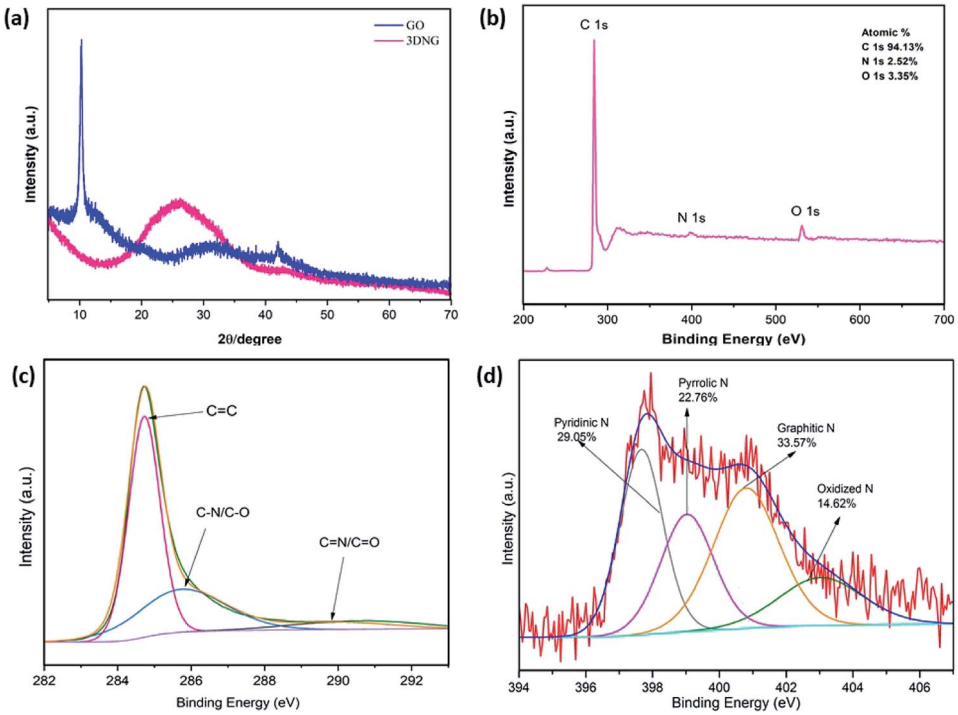

Fig. 3 (a) XRD patterns of GO and 3DNG; (b) XPS survey spectrum of 3DNG; high-resolution (c) C 1s and (d) N 1s spectra of 3DNG.

carbonyl and carboxyl (C═O) stretching groups and the skeletal vibrations of GO, and the peaks at around 1233 cm^{-1} and 1055 cm^{-1} were related to the hydroxyl COH and alkoxy C–O stretching vibrations of GO sheets.[23] After the N-doping during the thermal treatment, the oxygen-related groups disappeared or weakened as observed for the O–H groups at 3426 cm^{-1}; the GO was reduced by ascorbic acid and led to the absence of C═O peaks, and new peaks specific to C–N bonds emerged at 1185 cm^{-1} and C═C stretching bonds at 1569 cm^{-1}.[24] The 3DNG spectrum is shown in Fig. 2(b).

The XRD patterns of GO and 3DNG presented in Fig. 3(a) indicate that the GO sample has a typical peak at 10.2° (001) attributed to the lattice diffraction sheets. 3DNG demonstrated distinctive peaks, one at 26.5° due to the (002) carbon plane and another one at 43.2° corresponding to the (100)/(101) planes of graphitic carbon.[25,26] This indicated that GO oxide was reduced by ascorbic acid and the hydrothermal process by decomposing the C═O and COOR bonds in the GO sheets.[27] Furthermore, to examine the chemical content and the N and C species, XPS was performed on 3DNG. The 3DNG XPS survey in Fig. 3(b) shows three peaks belonging to C 1s, N 1s and O 1s at 284 eV, 400 eV

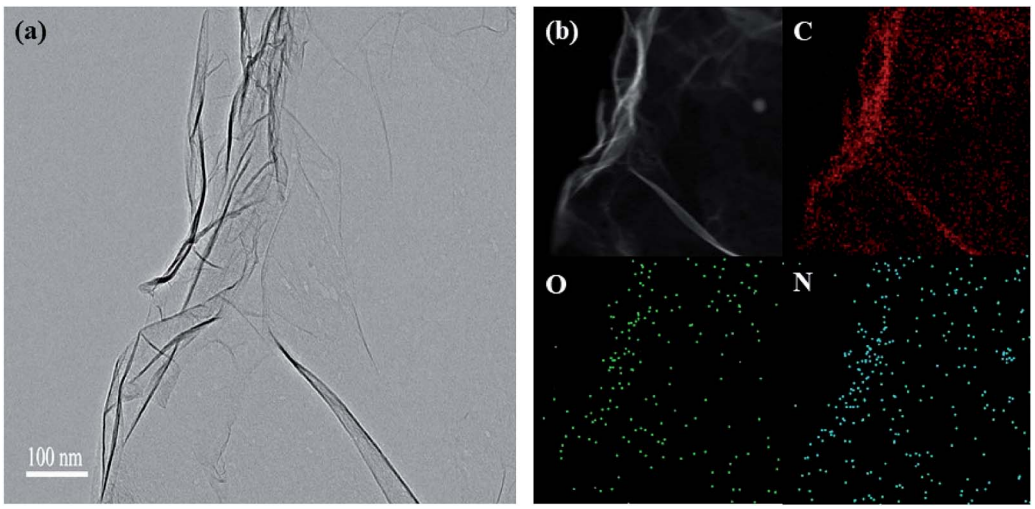

Fig. 4 (a) TEM image of 3DNG and (b) the corresponding elemental mappings of 3DNG.

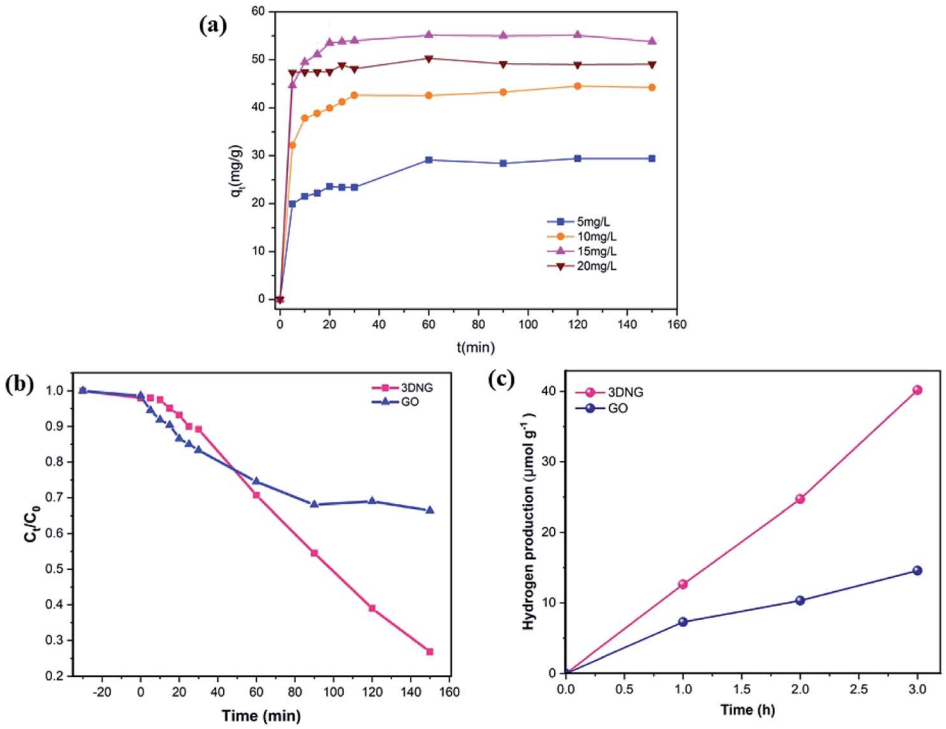

Fig. 5 (a) Time profile adsorption of 3DNG at different MB concentrations; (b) photocatalytic degradation of MB and (c) hydrogen production for GO and 3DNG.

and 532 eV, respectively, proving the successful N-doping. Fig. 3(c) shows the high-resolution C 1s spectrum, which could be related to 284.7 eV, 285.9 eV and 290.3 eV, attributed to C═C, C–N/C═O and C═N/C═O, respectively. Four distinct peaks ascribed to pyridinic N, pyrrolic N, graphitic N and N oxide at 397.6 eV, 399.7 eV, 400.5 eV and 403.0 eV, respectively, were observed as shown in Fig. 3(d),[28,29] indicating the successful doping of N in the 3DGN sample; these results concur with the FT-IR analysis. The 3DNG ratios were 0.035 for (O 1s)/(C 1s) and 0.026 for (N 1s)/(C 1s).

The TEM image of 3DNG (Fig. 4(a)) shows that it was composed of ultrathin transparent graphene nanosheets. The elemental mapping illustrated in Fig. 4(b) exposes the regular arrangement of C, O and N throughout the 3DNG, in accordance with the XPS survey that confirmed that N-element was efficiently doped into the 3D graphene structure.

To evaluate the photocatalytic activity of 3DNG, the adsorption property is a crucial factor that affects the photocatalytic performance. Fig. 5(a) shows the time profile of MB adsorption at different initial concentrations. The adsorption was fast during the first 20 min under all different concentrations, then started to stabilize and reached equilibrium after 60 min. The high adsorption property of 3DNG is probably due to the porous hierarchical structure, which provides efficient transport pathways and more available active adsorption sites.[32–35] The 3D structure possesses hydrogen bonding, which enhances the adsorption activity. Other important factors for the adsorption of methylene blue onto the 3D graphene are the electrostatic and π–π stacking interactions. These results have occurred in previous works that have proven the adsorption capacity of 3D graphene to eliminate cationic dyes.[2] The photocatalytic rate of 3DNG and GO was measured based on the MB degradation under visible-light irradiation. Fig. 5(b) shows that 3DNG has a higher photocatalytic degradation activity than GO, due to the synergistic effect of the 3D porous structure and the nitrogen dopant in the 3D graphene plane, favoring the charge carrier separation and high adsorption capacity for the structure of

Table 1 Comparison of the hydrogen production from recently reported works

Materials	Hydrogen production (3 h)	References
N-graphene	0 μmol g^{-1}	30
NGO-QDs	2 μmol g^{-1}	8
1% NGQDs-Cu_2O	34 μmol g^{-1}	31
3DNG	40 μmol g^{-1}	This work

Table 2 Comparison of the BET surface areas from recently reported work

Materials	BET surface	References
N-doped graphene aerogel	316 m^2 g^{-1}	36
N-doped graphene	156 m^2 g^{-1}	37
Ge-QD@NG/NGF3DNG	392 m^2 g^{-1}	38
3DNG	536 m^2 g^{-1}	This work

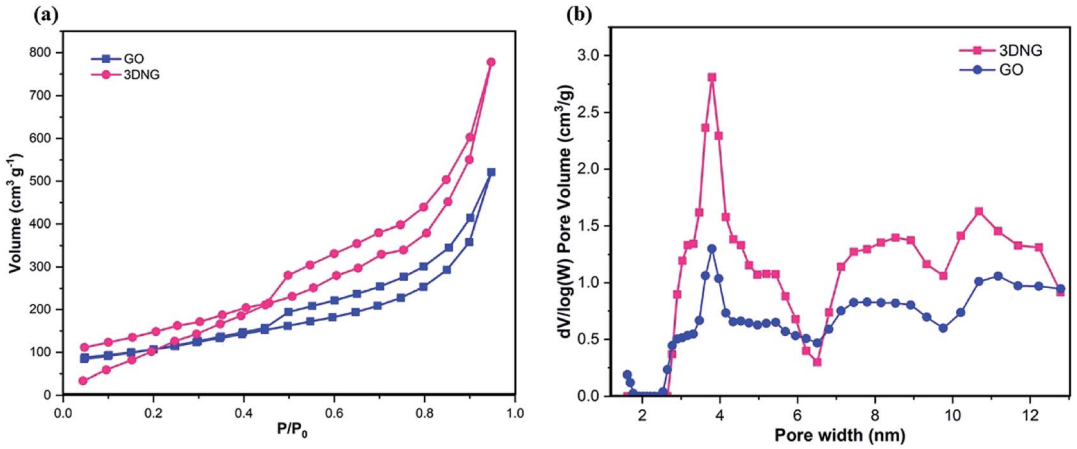

Fig. 6 (a) N_2 adsorption/desorption isotherms and (b) DFT pore size distributions of GO and 3DNG.

pollutants.[39,40] Moreover, the reduction of GO in 3DNG led to a conjugate aromatic structure that can catch the adsorbate *via* π–π interactions.[10] The high photoactivity is related to the enhanced adsorption due to the high contact of MB with 3DNG. The photocatalytic hydrogen production activities over GO and 3DNG were also investigated under visible-light irradiation to assess the structure and impact on the photocatalytic activity as indicated in Fig. 5(c). GO exhibited a photocatalytic hydrogen evolution of 14.579 μmol g^{-1} after 3 h of reaction, while the 3DNG demonstrated a higher hydrogen production of 40.182 μmol g^{-1} as compared to those reported for different graphene structures (Table 1). This provides further evidence of the promotion effect of the 3D structure and nitrogen-doping in graphene.

Nitrogen adsorption/desorption isotherms of GO and 3DNG are shown in Fig. 6(a). The type IV hysteresis loop of the isotherm curves suggests the presence of mesopores in GO and 3DNG,[41] which is evident from the mesoporosity centered at about 4.0 nm, exhibited by the DFT pore distribution (Fig. 6(b)). The mesopores connected to larger mesopores are considered to be responsible for the high surface area along with the porous structure that facilitates the mass transport, which corroborates previous work.[42–45] The surface area was calculated to be 364 m^2 g^{-1} for GO and 536 m^2 g^{-1} for 3DNG based on the multipoint Brunauer–Emmett–Teller (BET) method. The surface area of 3DNG is higher than previously reported works (Table 2), which accounts for the high adsorption of the 3DNG. Furthermore, nitrogen-doping is an important parameter for surface enlargement, which is helpful for the enhancement of the photocatalytic activity.

To further investigate the charge separation process, transient photocurrent responses and electrochemical impedance (EIS) were recorded. As shown in Fig. 7(a), under light irradiation, the photocurrent reached a high point followed by a quick decline, establishing a spike, then decreased progressively to reach a constant value. This spike is due to the separation of electron–hole pairs. The 3DNG exhibited a higher photocurrent response than GO; this

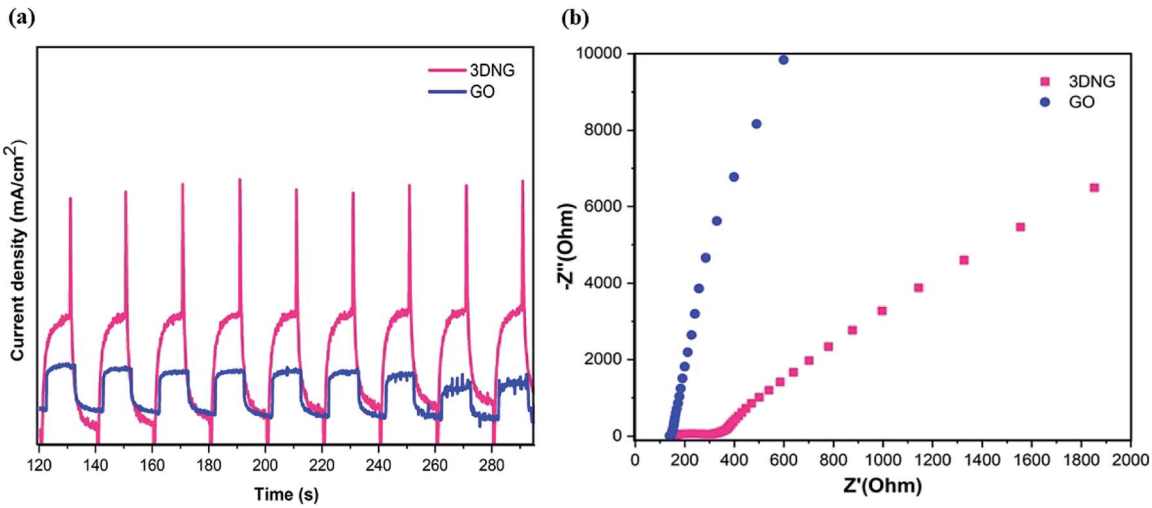

Fig. 7 (a) Transient photocurrent responses and (b) EIS curves of GO and 3DNG.

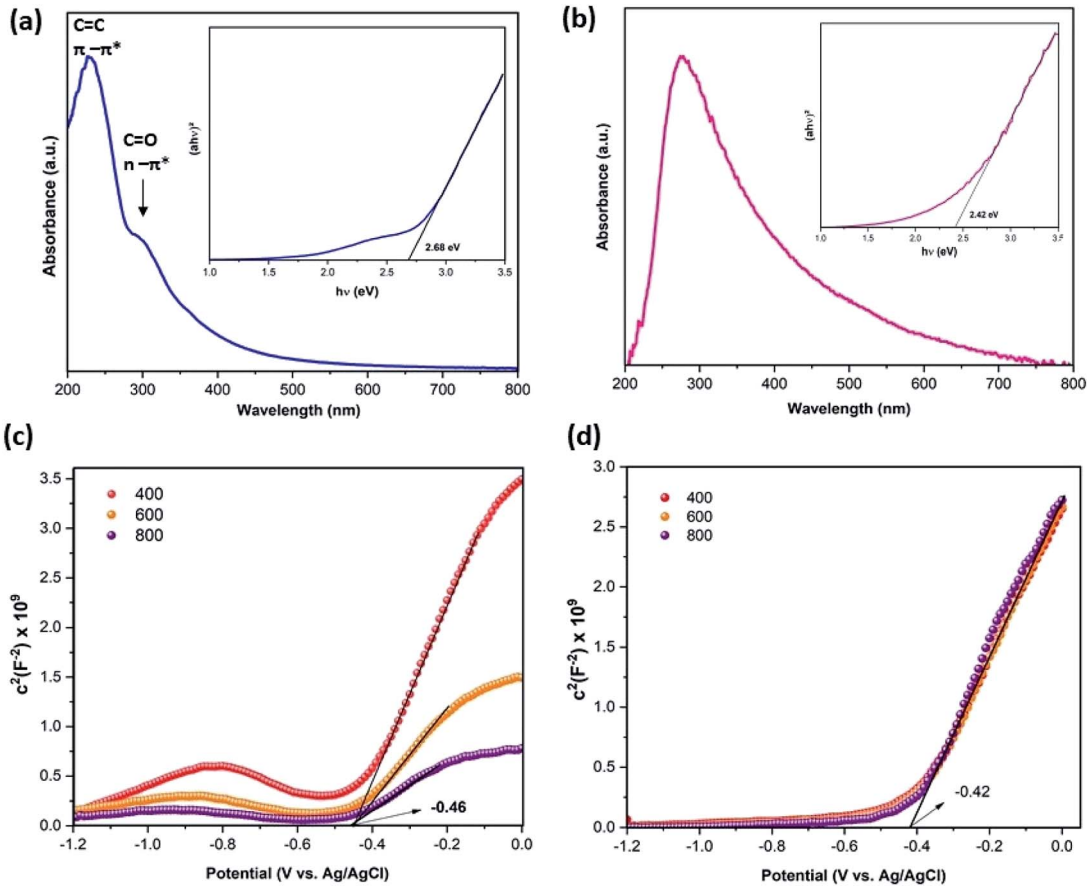

Fig. 8 (a) The UV-vis spectra of GO (inset: band gap of GO). (b) The UV-vis spectra of 3DNG (inset: band gap of 3DNG). (c) M–S plots over GO, (d) M–S plots over 3DNG.

improvement in photocurrent in 3DNG illustrates the fast charge separation.[46] Moreover, 3DNG has the smaller EIS semicircles radius (Fig. 7(b)), which is symbolic of a fast charge-transfer rate and low charge-transfer resistance due to the defects on the 3DNG surface. This makes the e^-–h^+ pair separation easier and leads to high photocatalytic efficiency.[47–49] The ultraviolet-visible absorption spectra were collected to clarify the optical properties and energy band gaps of GO and 3DNG. In Fig. 8(a), the absorption peak observed at 230 nm for GO is attributed to the π–π* transitions of C=C bonds, corresponding to an optical band gap of 2.68 eV determined using Tauc plot (inset Fig. 8(a)); the

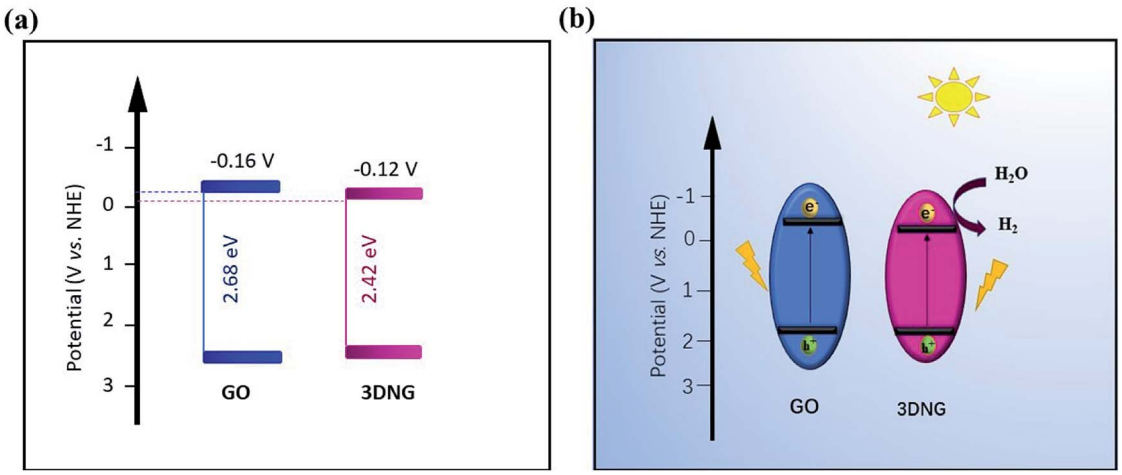

Fig. 9 (a) Energy level diagram and (b) mechanism of photocatalytic hydrogen production over GO and 3DNG.

small shoulder visible near 300 nm is attributed C=O bonds relative to n–π* transitions.[50] In contrast, the 3DNG showed an absorption peak at 276 nm relative to the π–π* transitions of C=C bonds as compared to an optical band gap of 2.42 eV (Fig. 8(b) and inset). The deoxygenation and restoration of the π-conjugation of GO led to a shift in the wavelength caused by the introduction of more lone electrons, which is typical of lone pairs of nitrogen and sp^2 hybridization. This shift provided 3DNG with a greater ability to absorb light in comparison to GO.[51] The obviously smaller band gap of 3DNG allows the absorption of visible light in an expanded range. The flat band potentials of GO and 3DNG were determined by the intercepts of the tangents of Mott–Schottky curves (Fig. 8(c and d)), which were −0.42 V for GO and −0.46 V for 3DNG (*vs.* Ag/AgCl, pH = 6.8). The flat band potentials were used to calculate the conduction band (CB) according to the following equation: $E_{fb} = E_{Ag/AgCl} + 0.059pH + E^{\theta}_{Ag/AgCl}$. Accordingly, the CB potential positions of GO and 3DNG were calculated to be −0.16 V and −0.12 V, respectively. Fig. 9(a) shows the energy level diagrams for GO and 3DNG based on the above results. For photocatalytic hydrogen production (Fig. 9(b)), under light irradiation, the photogenerated electrons of the 3DGN would jump from the valence band to the conduction band to react with water to produce H_2. The nitrogen dopant can accelerate the separation of the photogenerated carriers, and the 3D porous structure, with the presence of mesopores, can offer more active sites and favors the multi-light scattering/reflection, leading to the high photocatalytic performance of the 3DGN.[52,53]

Conclusions

A thermally treated 3D nitrogen-doped graphene aerogel with higher surface area (536 $m^2 g^{-1}$) and smaller band gap (2.42 eV) has been successfully synthesized using graphitic carbon nitride as the nitrogen source and graphene oxide (GO) as the skeleton. The 3D nitrogen-doped graphene aerogel demonstrated high MB adsorption capacity and enhanced methylene blue degradation and hydrogen production under the irradiation of visible light. Nitrogen doping with diverse nitrogenous moieties in graphene *via* thermal treatment and a 3D porous structure with enlarged specific area are believed to accelerate the charge separation for photocatalytic H_2 evolution and provide active sites for surface reaction. This work demonstrates that the 3D nitrogen-doped graphene aerogel with good adsorption is an efficient eco-friendly material for photocatalytic dye degradation and H_2 generation.

Conflicts of interest

There are no conflicts to declare.

Acknowledgements

This work was financially supported by the National Natural Science Foundation of China (Grant No. 51672112, 51702129 and 21972058), and Chinese Scholarship Council (2017GXZ026596). Y. Z. is thankful the support from Postdoctoral Science Foundation (2018M630527), China Scholarship Council (201708320150).

Notes and references

1 K. C. Lai, L. Y. Lee, B. Y. Z. Hiew, S. Thangalazhy-Gopakumar and S. Gan, *J. Environ. Sci.*, 2019, **79**, 174–199.
2 F. Zhang, Y.-H. Li, J.-Y. Li, Z.-R. Tang and Y.-J. Xu, *Environ. Pollut.*, 2019, **253**, 365–376.
3 P. Nikolaidis and A. Poullikkas, *Renewable Sustainable Energy Rev.*, 2017, **67**, 597–611.
4 Q. Jin, G. Xie, X. Cai, X. Hu, H. Wang, G. Qiu, W. Wang, D. Zhou, H. Huo, X. Tan and Y. Zhao, *RSC Adv.*, 2020, **10**, 6121–6128.
5 G. Liao, J. Fang, Q. Li, S. Li, Z. Xu and B. Fang, *Nanoscale*, 2019, **11**, 7062–7096.
6 E. Kusiak-Nejman, A. Wanag, J. Kapica-Kozar, Ł. Kowalczyk, M. Zgrzebnicki, B. Tryba, J. Przepiórski and A. W. Morawski, *Catal. Today*, 2019, DOI: 10.1016/j.cattod.2019.04.078.
7 W. Zhong, S. Shen, S. Feng, Z. Lin, Z. Wang and B. Fang, *CrystEngComm*, 2018, **20**, 7851–7856.
8 T.-F. Yeh, C.-Y. Teng, S.-J. Chen and H. Teng, *Adv. Mater.*, 2014, **26**, 3297–3303.
9 G. Liao, Y. Gong, L. Zhang, H. Gao, G.-J. Yang and B. Fang, *Energy Environ. Sci.*, 2019, **12**, 2080–2147.
10 B. Y. Z. Hiew, L. Y. Lee, X. J. Lee, S. Thangalazhy-Gopakumar, S. Gan, S. S. Lim, G.-T. Pan, T. C.-K. Yang, W. S. Chiu and P. S. Khiew, *Process Saf. Environ. Prot.*, 2018, **116**, 262–286.
11 Z. Zhuang, Y. Li, Z. Li, F. Lv, Z. Lang, K. Zhao, L. Zhou, L. Moskaleva, S. Guo and L. Mai, *Angew. Chem., Int. Ed.*, 2018, **57**, 496–500.
12 J. Wang, Z. Huang, W. Liu, C. Chang, H. Tang, Z. Li, W. Chen, C. Jia, T. Yao, S. Wei, Y. Wu and Y. Li, *J. Am. Chem. Soc.*, 2017, **139**, 17281–17284.
13 H.-P. Cong, J.-F. Chen and S.-H. Yu, *Chem. Soc. Rev.*, 2014, **43**, 7295–7325.
14 C. Lavorato, A. Primo, R. Molinari and H. Garcia, *Chem.–Eur. J.*, 2014, **20**, 187–194.
15 Z. Chen, Y. Zhang, L. Zhou, H. Zhu, F. Wan, Y. Wang and D. Zhang, *J. Hazard. Mater.*, 2017, **332**, 70–78.
16 C. Li, X. Li, X. Sun, X. Zhang, L. Duan, X. Yang, L. Wang and W. Lü, *Nanoscale Res. Lett.*, 2019, **14**, 249.
17 X. Chen, J. Wei, R. Hou, Y. Liang, Z. Xie, Y. Zhu, X. Zhang and H. Wang, *Appl. Catal., B*, 2016, **188**, 342–350.
18 D. C. Marcano, D. V. Kosynkin, J. M. Berlin, A. Sinitskii, Z. Sun, A. Slesarev, L. B. Alemany, W. Lu and J. M. Tour, *ACS Nano*, 2010, **4**, 4806–4814.
19 C. Maouche, Y. Zhou, B. Li, C. Cheng, Y. Wu, J. Li, S. Gao and J. Yang, *J. Electroanal. Chem.*, 2019, **853**, 113536.
20 M. Kumar, T. Kesavan, G. Kalita, P. Ragupathy, T. Narayanan and D. Pattanayak, *RSC Adv.*, 2014, **4**, 38689–38697.
21 S. Dai, Z. Liu, B. Zhao, J. Zeng, H. Hu, Q. Zhang, D. Chen, C. Qu, D. Dang and M. Liu, *J. Power Sources*, 2018, **387**, 43–48.

22 B. Vinayan, R. Nagar and R. Sundara, *J. Mater. Chem.*, 2012, **22**, 25325–25334.
23 Y. Yang, L. Xu, H. Wang, W. Wang and L. Zhang, *Mater. Des.*, 2016, **108**, 632–639.
24 M. Ge, H. Hao, Q. Lv, J. Wu and W. Li, *Electrochim. Acta*, 2019, 135236, DOI: 10.1016/j.electacta.2019.135236.
25 G. Panomsuwan, N. Saito and T. Ishizaki, *Mater. Today: Proc.*, 2015, **2**, 4302–4308.
26 P. Chen, T. Zhou, L. Xing, K. Xu, Y. Tong, H. Xie, L. Zhang, W. Yan, W. Chu, C. Wu and Y. Xie, *Angew. Chem., Int. Ed.*, 2017, **56**, 610–614.
27 M. A. Basith, R. Ahsan, I. Zarin and M. A. Jalil, *Sci. Rep.*, 2018, **8**, 11090.
28 Y. Li, J. Yang, N. Zhao, J. Huang, Y. Zhou, K. Xu and N. Zhao, *Appl. Catal., A*, 2017, **534**, 30–39.
29 H. Xu, L. Ma and Z. Jin, *J. Energy Chem.*, 2018, **27**, 146–160.
30 J.-B. Baek and D. Chang, *Chem.–Asian J.*, 2016, 11.
31 Y. Wu, M. Yan, J. Gao, P. Lv, X. Liu, C. Li and Y. Yan, *Nano*, 2018, **13**, 1850099.
32 H. Tang, H. Huang, X. Wang, K. Wu, G. Tang and C. Li, *Appl. Surf. Sci.*, 2016, **379**, 296–303.
33 B. Fang, J. H. Kim, M.-S. Kim and J.-S. Yu, *Acc. Chem. Res.*, 2013, **46**, 1397–1406.
34 B. Fang, M. Kim, S.-Q. Fan, J. H. Kim, D. P. Wilkinson, J. Ko and J.-S. Yu, *J. Mater. Chem.*, 2011, **21**, 8742–8748.
35 B. Fang, J. H. Kim, C. Lee and J.-S. Yu, *J. Phys. Chem.C*, 2008, **112**, 639–645.
36 J. Zhang, C. Li, Z. Peng, Y. Liu, J. Zhang, Z. Liu and D. Li, *Sci. Rep.*, 2017, **7**, 4886.
37 A. I. Pruna, A. C. Cárcel, A. Benedito and E. Giménez, *Nanomaterials*, 2019, **9**, 350.
38 R. Mo, D. Rooney, K. Sun and H. Y. Yang, *Nat. Commun.*, 2017, **8**, 13949.
39 J. Gogoi, A. D. Choudhury and D. Chowdhury, *Mater. Chem. Phys.*, 2019, **232**, 438–445.
40 A. R. Khataee and M. B. Kasiri, *J. Mol. Catal. A: Chem.*, 2010, **328**, 8–26.
41 J. Huang, J. Han, T. Gao, X. Zhang, J. Li, Z. Li, P. Xu and B. Song, *Carbon*, 2017, **124**, 34–41.
42 X. Chen, Y. Liang, L. Wan, Z. Xie, C. D. Easton, L. Bourgeois, Z. Wang, Q. Bao, Y. Zhu, S. Tao and H. Wang, *Chem. Eng. Sci.*, 2019, **194**, 36–44.
43 Q. Wei, G. Zhang, X. Yang, R. Chenitz, D. Banham, L. Yang, S. Ye, S. Knights and S. Sun, *ACS Appl. Mater. Interfaces*, 2017, **9**, 36944–36954.
44 J. H. Kim, B. Fang, M. Kim and J.-S. Yu, *Catal. Today*, 2009, **146**, 25–30.
45 W.-B. Hua, X.-D. Guo, Z. Zheng, Y.-J. Wang, B.-H. Zhong, B. Fang, J.-Z. Wang, S.-L. Chou and H. Liu, *J. Power Sources*, 2015, **275**, 200–206.
46 H. Meng, T. Wang, X. yu, Y. Zhu and Y. Zhang, *RSC Adv.*, 2015, **5**, 107088–107097.
47 Q. Liu, J. Shen, X. Yu, X. Yang, W. Liu, J. Yang, H. Tang, H. Xu, H. Li, Y. Li and J. Xu, *Appl. Catal., B*, 2019, **248**, 84–94.
48 W. Zhong, S. Shen, M. He, D. Wang, Z. Wang, Z. Lin, W. Tu and J. Yu, *Appl. Catal., B*, 2019, **258**, 117967.
49 W. Zhong, J. Huang, S. Liang, J. Liu, Y. Li, G. Cai, Y. Jiang and J. Liu, *ACS Energy Lett.*, 2020, **5**, 31–38.
50 K. R. Geethalakshmi, T. Y. Ng and R. Crespo-Otero, *J. Mater. Chem.*, 2016, **4**, 8429–8438.
51 N. Ngidi, M. Ollengo and V. Nyamori, *Materials*, 2019, **12**, 3376.
52 B. Fang, Y. Xing, A. Bonakdarpour, S. Zhang and D. P. Wilkinson, *ACS Sustainable Chem. Eng.*, 2015, **3**, 2381–2388.
53 B. Fang, A. Bonakdarpour, K. Reilly, Y. Xing, F. Taghipour and D. P. Wilkinson, *ACS Appl. Mater. Interfaces*, 2014, **6**, 15488–15498.